Electrothermal behavior and terahertz emission properties of a planar array of two $Bi_2Sr_2CaCu_2O_{8+\delta}$ intrinsic Josephson junction stacks

2015 Supercond. Sci. Technol. 28 055004

(http://iopscience.iop.org/0953-2048/28/5/055004)

IOP Publishing Superconductor Science and Technology
Supercond. Sci. Technol. **28** (2015) 055004 (10pp) doi:10.1088/0953-2048/28/5/055004

Electrothermal behavior and terahertz emission properties of a planar array of two $Bi_2Sr_2CaCu_2O_{8+\delta}$ intrinsic Josephson junction stacks

B Gross[1], F Rudau[1], N Kinev[2], M Tsujimoto[1,3], J Yuan[4], Y Huang[4,5], M Ji[4,5], X J Zhou[4,5], D Y An[5], A Ishii[4], P H Wu[5], T Hatano[4], D Koelle[1], H B Wang[4,5], V P Koshelets[2] and R Kleiner[1]

[1] Physikalisches Institut—Experimentalphysik II and Center for Collective Quantum Phenomena in LISA$^+$, Universität Tübingen, Auf der Morgenstelle 14, D-72076 Tübingen, Germany
[2] Kotel'nikov Institute of Radio Engineering and Electronics, Moscow, Russia
[3] Kyoto University, Kyoto, Japan
[4] National Institute for Materials Science, Tsukuba 3050047, Japan
[5] Research Institute of Superconductor Electronics, Nanjing University, Nanjing 210093, People's Republic of China

E-mail: borisgross@arcor.de

Received 30 November 2014, revised 11 February 2015
Accepted for publication 22 February 2015
Published 19 March 2015

Abstract

We report on the investigation of the electrothermal behavior and the terahertz (THz) emission properties of two nearby $Bi_2Sr_2CaCu_2O_{8+\delta}$ (BSCCO) intrinsic Josephson junction stacks, using a combination of electric transport and THz emission measurements plus low temperature scanning laser microscopy. We start with a compact BSCCO stack (placed in a z-shaped structure between two BSCCO electrodes) with lateral dimensions of $330 \times 60\ \mu m^2$ and $0.7\ \mu m$ height, consisting of about 480 junctions. After characterization, a 200 nm wide slit was introduced by focused ion beam milling, splitting the stack into two halves connected by continuous superconducting electrodes. In a third step, the upper electrode was also split, leading to a structure where the two stacks can be biased separately. In all configurations hot-spot formation was observed. Despite the separation into two stacks only a single hot spot formed, which, depending on the bias condition, could either be located in one of the stacks or extend into both stacks with its center in the slit. In none of the structures it was possible to achieve mutual synchronization of the two stacks, indicating that additional synchronizing elements or the presence of a base crystal as for mesa structures may be necessary for the operation of parallel array structures.

Keywords: intrinsic Josephson junction, terahertz, high temperature superconductor

(Some figures may appear in colour only in the online journal)

1. Introduction

Josephson junctions are attractive sources of radiation because of the fact that the emitted frequency f_e is tunable by an applied dc voltage V, following the relation $f_e = V/\Phi_0$, where $\Phi_0 = 2.07 \times 10^{-15}$ Wb is the flux quantum. One obtains an emission frequency of 483.6 GHz per mV of applied voltage. There are, however, several drawbacks. A single junction delivers only very little power, usually well below 1 nW. Also, a typical junction has a low impedance and is not well matched to the environment. Using conventional superconductors such as Nb these problems have been

overcome by using 1D or 2D arrays of Josephson junctions oscillating coherently, see e.g. [1–3]. Ideally the emission power increases quadratically with the junction number.

In 2007 it has been shown that intrinsic Josephson junctions (IJJs) [4] in the high temperature superconductor $Bi_2Sr_2CaCu_2O_{8+\delta}$ (BSCCO) can emit coherent radiation at THz frequencies [5]. Here, stacks of hundreds of IJJs have been patterned as a mesa structure on the surface of a BSCCO single crystal. A typical mesa has a length of ~300 μm, a width around 30–80 μm and a thickness of about 1 μm, corresponding to a serial array of about 670 IJJs. Although the power emitted into free space was below 1 μW in these initial experiments, it triggered numerous experimental [6–27] and theoretical [28–49] investigations; for recent reviews, see [17, 50, 51]. IJJ stacks have been realized as mesa structures, a pedestal standing on top of a base crystal, but also as more sophisticated structures like bare IJJ stacks contacted by Au layers [17, 19, 23] and as all-superconducting z-shaped structures [12]. For the best stacks, emission powers in the range of tens of μW have been achieved [19, 20, 23].

Due to their poor thermal conductivity IJJ stacks are subject to enormous self-heating [5–7, 10, 16, 20, 22, 25, 39, 44–46], causing the formation of hot spots, i.e. regions heated to temperatures above the superconducting transition temperature T_c. Hot-spot formation in IJJ stacks has been imaged by low temperature scanning laser microscopy (LTSLM) [6, 8, 10], by thermoluminescence [20, 22, 25] and has been analyzed theoretically using heat-diffusion equations [39, 40, 44, 45]. There is still some debate to what extent the presence of a hot-spot is helpful or not for THz emission [25, 27]. For example, in its presence the linewidth of radiation is much lower than in its absence [13, 24]. On the other hand Joule heating limits the maximum voltage V per junction that can be achieved. At low bias currents (low-bias regime) the voltage across the IJJ stack increases with increasing current. For large enough currents the self-heating leads to a decrease in the c-axis resistance and finally a back-bending of the current–voltage characteristic (IVC). In this regime of negative differential resistance (high-bias regime) hot-spot formation occurs in a similar way as it also has been observed in other conductors having a negative temperature coefficient of their resistance [52]. For a stack consisting of $N \sim 1000$ IJJs one typically obtains a maximum voltage per junction $V_{\max}$ of about 1.5–2 mV, limiting the emission frequency to values below 1 THz. If one would increase N to much larger numbers, $V_{\max}$ would decrease further, making IJJ stacks inattractive for THz emission.

Although proposals [40] and experimental attempts [53] have been made to provide better cooling, the best way to increase the emission power while keeping $V_{\max}$ reasonably large is to use planar arrays of IJJ stacks [21, 27, 47, 54]. Recently, arrays of 8 parallel mesas have been realized [21]. It was possible to synchronize up to three stacks of the array and achieve an output power of 0.61 mW at an emission frequency of 0.51 THz. Evidence for synchronized emission in this work and in [54] was provided by the scaling of the emission power with the square of the junction number. On the other hand, the strong heating evident in these samples may have affected the radiation impedance of each stack, making statements about a scaling with the junction number difficult. In addition it is important to find out more details about the mechanism of synchronization, e.g., whether it is purely electromagnetic in origin, or caused (or assisted) by thermal currents.

To address such issues we have investigated the electrothermal behavior and the emission properties of the simplest possible array—two stacks in parallel. We have chosen all-superconducting z-structures which, on the one hand are easy to manipulate and, on the other hand have the potential for integrating a large number of stacks [55].

For our investigation we started with a IJJ stack in a z-shaped BSCCO structure. After characterization, using focused ion beam (FIB) milling we cut a slit into the stack splitting it into two halves, which were still connected in parallel by continuous electrodes. Having characterized this geometry we cut the upper electrode via FIB.

The reminder of this paper is organized as follows. In section 2 we describe the fabrication process and the measurement techniques. Section 3.1 presents and analyses data for the sample before FIB milling, and in sections 3.2 and 3.3 results are presented for the sample after the first and the second milling process, respectively. We discuss the results in section 4 and conclude with section 5.

2. Samples and measurement techniques

The IJJ stack we study has been fabricated using a double-sided technique as described in [12]. In brief, a 30 nm thick gold layer was deposited on a freshly cleaved, slightly underdoped BSCCO single crystal, which has been glued to a substrate with epoxy prior to this. The superconducting transition temperature of the crystal is $T_c = 87$ K. A pre-structure was patterned into the surface with optical lithography and argon ion milling. Subsequently, the structure was turned upside down and glued to a second substrate. The first substrate was removed and the BSCCO surface was cleaved until the desired thickness of the remaining crystal was reached. Now the final structure of the IJJ stack was patterned into the crystal and covered by a protecting gold layer of 30 nm.

In contrast to mesas standing on top of a base crystal, the electrodes connecting the stack are superconducting, allowing real four-terminal measurements. The electrodes typically have a thickness of less than 1 μm. The stack we investigate is designed in an overlap geometry as sketched in figures 1(a) and (b). The stack has dimensions of $330 \times 60 \times 0.7$ μm^3 and consists of about 480 IJJs. After performing electric transport, LTSLM and THz detection measurements (for details, see below), the sample was modified in an additional patterning step. Using FIB milling the IJJ stack was cut into two halves of almost equal size, separated by a slit of around 200 nm in width, cf figure 1. The two stacks still share the same superconducting electrodes and are connected in parallel. Thus, this sample can be understood as a very simple array structure, appropriate for studying generic features of arrays.

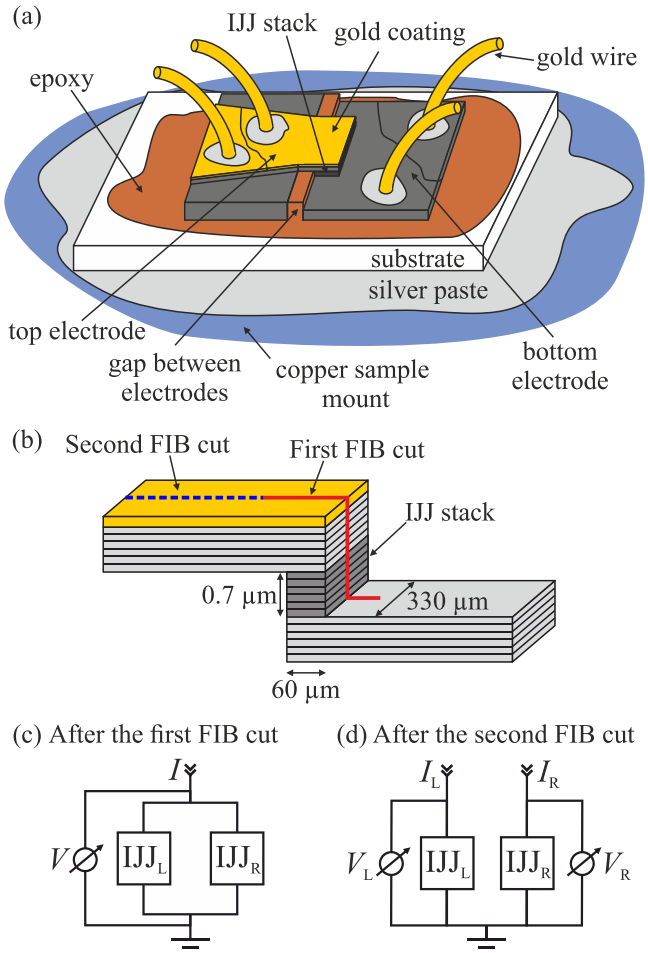

Figure 1. (a) Sketch of a BSCCO IJJ overlap structure fabricated with the double-sided technique. (b) The red and the dashed blue line indicate the two FIB cuts in an enlarged view of the overlap structure. The block diagrams show the electric biasing scheme of the IJJ stacks after (c) the first and (d) the second FIB milling step.

After investigating this configuration by electric transport, LTSLM and THz detection, the top electrode of the two stacks was separated in a second FIB milling step, making the bias currents of the stacks independent of each other.

The setup for LTSLM is described in [56]. In brief, the beam of a laser diode is focused and scanned across the sample surface. The induced local heating at position (x_0, y_0) of about $\Delta T \approx$ 2–3 K in an area A_L of a few μm^2 and a depth of about 0.5 μm leads to a voltage change $\Delta V(x_0, y_0)$ across the IJJ stack, which serves as contrast for the LTSLM image. In particular, the temperature distribution in the stack can be reconstructed from this signal, based on the impact of the local heating on the c-axis quasi-particle transport, see [44]. The signal is given by

$$\Delta V(x_0, y_0) \approx \frac{-IR_{\mathrm{eff}}^2 \Delta T A_L}{h} \frac{\mathrm{d}\sigma_c}{\mathrm{d}T}\Big(T(x_0, y_0)\Big). \qquad (1)$$

$R_{\mathrm{eff}} = V/I$ is the (ohmic) sample resistance at a given current I. $\mathrm{d}\sigma_c/\mathrm{d}T$ denotes the temperature derivative of the c-axis electrical conductivity and h is the sample thickness. For better comparability of LTSLM signals at different bias points we introduce a normalized voltage signal

$$\Delta V_{\mathrm{norm}} = \Delta V / \left(IR_{\mathrm{eff}}^2\right). \qquad (2)$$

The THz detection setup, allowing for bolometric detection and for Fourier spectrometry, is described in detail in the supplement of [8]. The crystal is mounted in a continuous flow cryostat with a polyethylene window. The emitted radiation, chopped with a frequency of 80 Hz, is collected by a 90° of f-axis parabolic mirror (2″ diameter, focal length 10 cm) and deflected towards two lamellar split mirrors, which divide the incoming radiation into two beams with almost equal intensity. A phase difference is introduced by moving one of these mirrors with a translation stage. Via a second parabolic mirror the radiation is deflected to the bolometer. A 3 THz cut-off type filter is used in front of the bolometer. The frequency resolution, depending on the maximum mirror displacement, is 10–15 GHz. During the measurements of the data for the present paper we have improved the positioning unit for the IJJ stack. Therefore, the bolometric signal detected from the pristine stack is significantly smaller than for later measurements.

We also performed some measurements of THz radiation using a superconducting Nb/AlN/NbN integrated receiver (SIR) for detection, which is able to resolve the linewidth of the THz radiation [13]. The SIR comprises, on a single chip, a planar antenna combined with a superconductor-insulator-superconductor (SIS) mixer, a superconducting flux-flow oscillator (FFO) acting as local oscillator, and a SIS harmonic mixer for the FFO phase locking. The frequency of the local oscillator is continuously tunable from 350 to 750 GHz, while the SIS mixer is effectively matched to the planar antenna between 450 and 700 GHz, limiting the SIR operation range. A frequency resolution of the SIR well below 100 kHz has been confirmed [57].

3. Results

3.1. Pristine stack

We first discuss data, as taken from the pristine, i.e. uncut, stack.

3.1.1. Electric properties and THz emission. The black (red) graph in figure 2(a) shows the measured IVC for the pristine sample at a bath temperature of T_b = 42 K in the high (low) bias regime. Apart from the absence of a contact resistance the IVC is similar to the IVCs of comparably sized mesa structures, showing the typical back bending at high input power. The maximum voltage per junction V_{max} is about 1.4 mV and thus roughly the same as for mesa structures. In fact, because of the significantly thinner bottom electrode of this structure compared to a base crystal one might expect a better thermal coupling to the bath and a larger V_{max}. This is

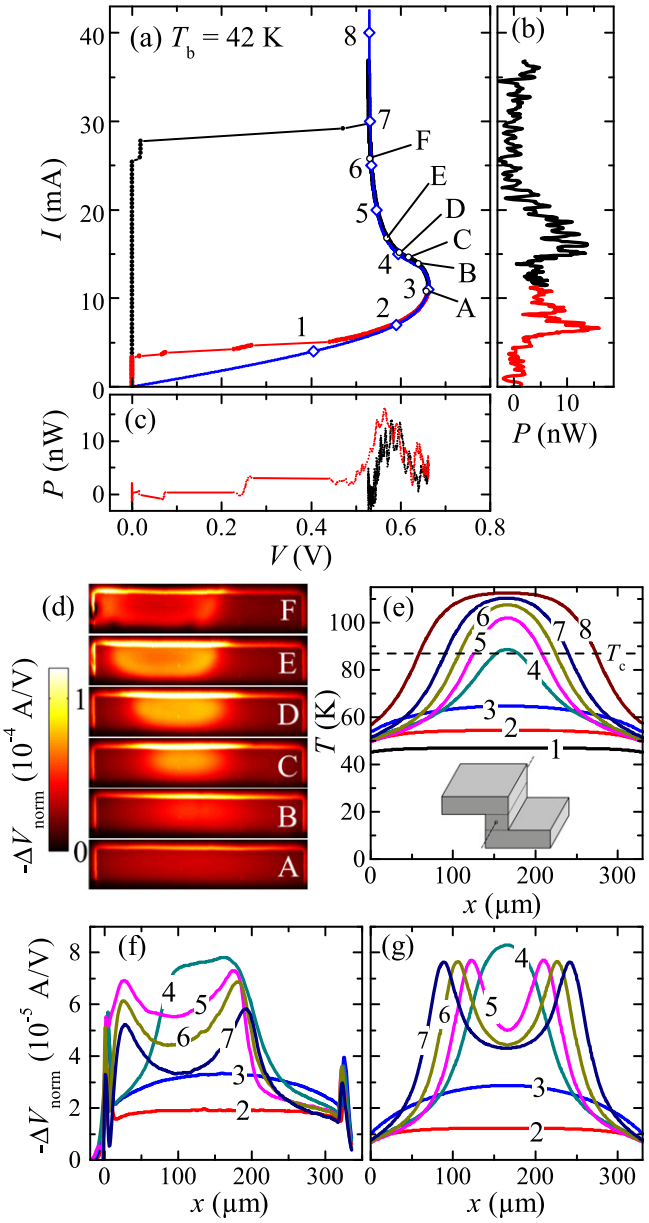

Figure 2. Data of the pristine overlap structure at T_b = 42 K. (a) Measured (black—high bias, red—low bias) and simulated (blue) IVCs. Detected radiation signal versus (b) current and (c) voltage, color code as in (a). (d) LTSLM images recorded for the bias points A–F marked in (a). (e) Simulated $T(x)$-profiles along the line indicated in the inset for the bias points 1–8 marked in (a). Measured (f) and simulated (g) LTSLM voltage responses for the same linescan and bias points as the $T(x)$-profiles in (e).

not observed, indicating that the glue layer is the bottleneck for the thermal coupling to the bath.

Figures 2(b) and (c) display the bolometric radiation signal depending on (b) the current through and (c) the voltage across the stack. Since the sample was somewhat out of focus the overall signal is comparatively small. Still, one clearly observes that there are relatively broad emission peaks both in the high- and low-bias region. Plotted as a function of voltage these peaks nearly coincide, cf figure 2(c). For the low-bias emission power peak at around V = 565 mV our THz spectrometer showed an emission frequency f_e = 562 GHz. In the high-bias regime, the emission power peaks around 580 mV with f_e = 577 GHz. For both peaks the Josephson relation gives a junction number $N \approx 487$, indicating that basically all junctions in the stack participate in radiation.

3.1.2. Electrothermal properties. Figure 2(d) shows a series of LTSLM images taken at bias points A–F in figure 2(a). At bias point A only a smooth voltage response is seen which becomes peaked in images B and C, indicating that a hot spot has formed near the center of the stack. With increasing bias current the hot spot moves towards the left and grows in size, cf images D, E and F. This behavior is somewhat different from hot-spot formation in mesa structures. Mesas are typically electrically contacted with a wire attached to the the mesa surface by silver paste. The hot spot forms near the contact point, although it prefers, in principle, the point of worst cooling [44]. For the double-sided structure there is no contacting wire and thus, not surprizingly, the hot spot initially forms near the center of the stack.

To model the IVC and the temperature distribution in the stack we solved the nonlinear heat diffusion equation with finite element analysis as in [44], accounting as good as possible for the real geometry and the electrical and thermal parameters of the materials involved. The thickness of the electrodes was taken to be 0.8 μm, the gap between top and bottom electrode was 20 μm, the thickness of the glue layer 20 μm and the gold layer 30 nm, respectively. The current was injected through the large surface of the upper electrode by defining a corresponding boundary condition. Equally, the ground is defined on the bottom electrode. The calculated IVC is shown by the blue curve in figure 2(a). For this curve the subgap c-axis resistivity $\rho_c(T)$ of BSCCO below T_c, which eludes experimental access in our case, has been adjusted until measured and simulated IVC showed a good agreement. For all other simulated curves shown below this $\rho_c(T)$ has been used without further modification. Figure 2(e) shows the simulated $T(x)$-profiles along the line indicated in the inset for the bias points labelled 1–8 in figure 2(a). While for bias points 1–3 only a smooth temperature distribution is seen, at point 4 a hot spot has formed, which grows in size and increases in temperature with increasing bias current, reaching peak temperatures well above T_c.

To compare experiment and simulation we first show experimental linescans of the LTSLM response in figure 2(f), for the bias points 2–7 in figure 2(a). The linescans are taken along the center of the stack, see the line in the inset of figure 2(e). While the linescans 2 and 3 are relatively smooth, for the bias points 4–7 they show the characteristic double-peak structure which is observed in the presence of hot spots. The LTSLM response is given by equation (1), i.e. it only indirectly yields the temperature distribution in the stack. To compare this with theory, rather than inverting the experimental curves to obtain $T(x)$ we have used the calculated temperature profiles of figure 2(e) to calculate the normalized LTSLM response from equation (2). The result is shown in figure 2(g). The measured response is reproduced well, except

for the drift of the hot spot to the left. This drift is presumably due to local inhomogeneities arising e.g. from a varying thickness of the glue layer, which is not incorporated in the simulations. We also observe that the LTSLM response is stronger at the sample edges. This originates in the absence of the protecting gold layer, a side effect of the fabrication process, leading to increased heating by the laser. The characteristic double-hump feature of the hot spot stems from the presence of a maximum in $d\sigma_c/dT\,(T)$ close to $T = T_c$, reducing the response signal for temperatures above T_c. Also note, that the normalization by $IR_{\rm eff}^2$ seems not to fully compensate a signal reduction for increasing input power, compare linescans 5–7 with the simulated equivalents.

3.2. Two parallel stacks

We now study the overlap structure after adding the slit, as shown in figures 1(b) and (c).

3.2.1. Electric properties and THz emission. Figure 3(a) shows by black (low-bias regime), red (region of negative differential resistance) and blue (region of positive differential resistance at high bias) curves the IVC of the double stack for T_b = 42 K and voltages between 0.45 and 0.7 V, in comparison with the IVC of the pristine overlap structure (dark green and orange symbols, denoting low- and high-bias region, respectively). The inset of figure 3(a) shows the IVCs of the pristine and cut sample on a wider voltage scale. One notes that in comparison to the pristine stack, the backbending between 10 and 25 mA of the resistive branch became stronger. Further, the IVC now has positive differential resistance above 25 mA in contrast to negative differential resistance before. Quite surprisingly, as a new feature a hysteresis appears for currents between 38 and 45 mA. The detected radiation signal for the cut sample is shown in figure 3(c) versus current and (e) versus voltage, in comparison with the radiation signal detected for the pristine sample, cf figures 3(b) and (d). As before milling, the sample shows emission both for low bias currents and in the hot spot nucleation regime, with emission frequencies between 596 and 506 GHz, i.e. at comparable frequencies as in the pristine case. In addition, for high bias currents (between 30 and 40 mA) emission peaks appear which did not exist before with frequencies of about 550 GHz. Likely, the origin of these new emission peaks is the positive differential resistance occuring in this regime, which directs the IVC to the voltage range that allowed for strong THz emission at lower currents. As we will see below, in this part of the IVC one of the stacks is at a temperature above T_c, while the other stack is still superconducting, although at a (inhomogeneous) temperature which is significantly above T_b. All of the determined frequencies, indicated by numbers in GHz in figures 3(b) and (c), obey the Josephson relation $f_e = V/(N\Phi_0)$, with $N \approx 481$ within measurement accuracy.

In the interferometer measurements the linewidth is resolution limited to around 15 GHz and always one single emission line is detected. It is not resolved, if both stacks emit coherently at the same frequency, if they emit slightly detuned

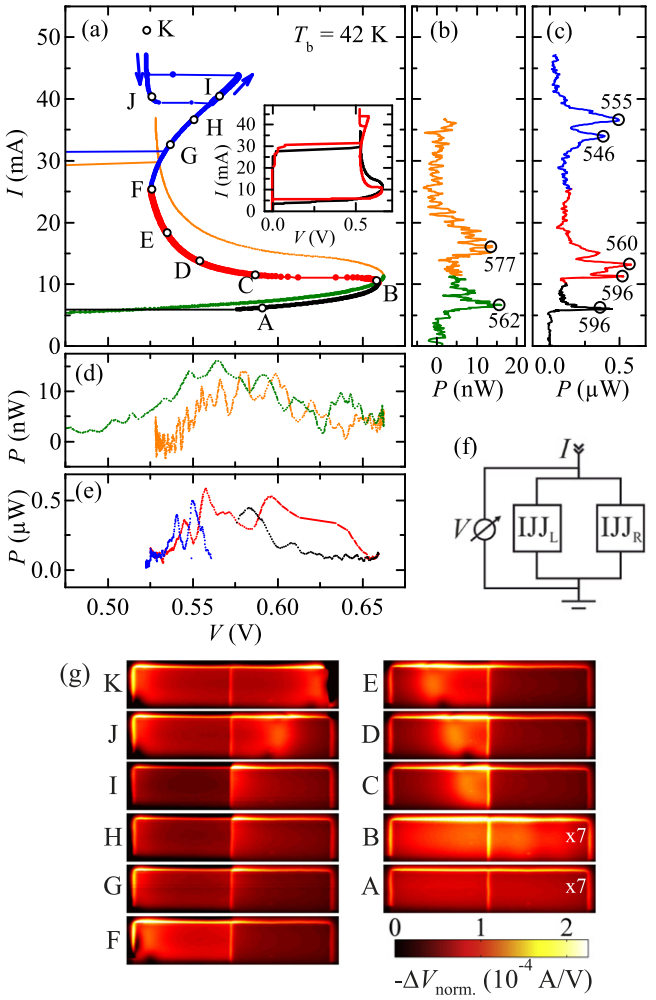

Figure 3. Comparison of data before and after FIB milling for T_b = 42 K: (a) IVCs on different voltage scales. Detected radiation signal versus (b), (c) current and (d), (e) voltage. In (a) the low- and the high-bias regimes of the pristine stack are indicated by dark green and orange colors, respectively. For the IVC of the stack after FIB milling the low-bias regime is indicated by black symbols. Red symbols indicate the region of negative differential resistance and blue symbols the region of positive differential resistance at high bias. Graphs (b) and (d) are for the pristine stack, (c) and (e) for the stack after FIB milling, using the same color code as in (a). Numbers in (b) and (c) are measured radiation frequencies in GHz. In (f) the equivalent electric circuit is depicted schematically. (g) LTSLM images for the stack after FIB milling, taken at bias points A–K indicated in (a). For a better comparison, the signals in the images A and B were multiplied by a factor of 7.

within the resolution, or if only one stack emits. To resolve this, we also performed some linewidth measurements at T_b = 42 K with the SIR. Similar measurements on mesa structures are described in [13]. For all SIR measurements on the overlap structure with two stacks in parallel two frequency lines were observed in the low-bias regime as well as in the back-bending regime. The observed separation between the two emission lines ranged from some ten MHz to several GHz. The linewidth of radiation varied in the low-bias regime between 162 and 568 MHz and in the back-bending regime between 43 and 271 MHz. The smaller values of Δf in the presence of a hot spot are compatible with the measurements

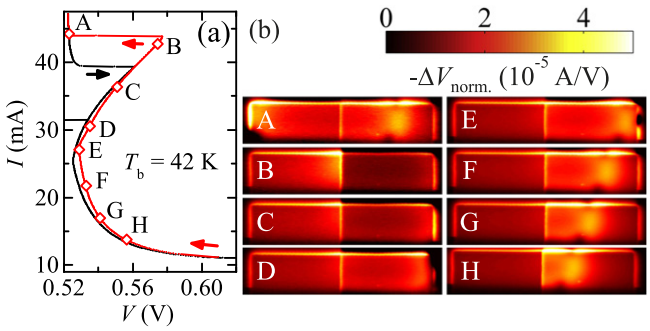

Figure 4. Data after FIB milling at $T_b = 42$ K (a) IVC for normal (black) and reverse (red) hot-spot formation. (b) LTSLM images for the bias points indicated in (a).

in [13] for a standard mesa. Thus, the two stacks did not emit coherently and even worse, the frequency of oscillation was slightly different in the two stacks despite the fact that they were connected by continuous superconducting electrodes.

3.2.2. Electrothermal properties. To analyze the electro-thermal behavior we show in figure 3(g) LTSLM images for the bias points labelled A–K in figure 3(a). While in images A and B the LTSLM signal is almost homogeneous, in images C to F it is seen that hot-spot formation takes place in the left stack, rather than in the center, as for the pristine stack. The hot spot nucleates directly at the slit milled by FIB technique. With increasing current its center moves towards the center of the left stack and simultaneously grows in size until it eventually covers the complete left stack. In the regime of positive differential resistance in the IVC the hot spot starts to extend to the stack right of the slit (cf images G–I), however, only after a jump in the IVC it really covers a significant part of the right stack, as seen in image J. At bias point K both stacks seem to be completely occupied by the hot spot. In this state, i.e. for bias currents between images J and K no THz emission was observed.

We also note that, since the two stacks are almost equally sized, one might expect that the initial hot-spot formation can also occur in the right stack. Indeed we were able to realize this by keeping the bias current at around 11 mA, where dI/dV approaches almost zero and the system is quite unstable. By chance, one or the other configuration is realized, when the current is increased. The IVC follows a slightly different path in the reverse hot spot configuration. See figure 4(a) for the corresponding IVCs and (b) for the LTSLM images showing the reverse hot spot formation.

For a first understanding of the electro-thermal properties of the sample after FIB milling we note that with the slit the in-plane heat flow through the stack is interrupted. The situation resembles the discrete resistor model [44, 58, 59] where it has been found that, compared to a symmetric temperature distribution, one of the resistors can get hot while the other becomes colder. In our geometry the two stacks are spatially distributed, but the same mechanism should lead to a symmetry broken state. For a more quantitative analysis we solved the heat diffusion equation for the slit geometry, using

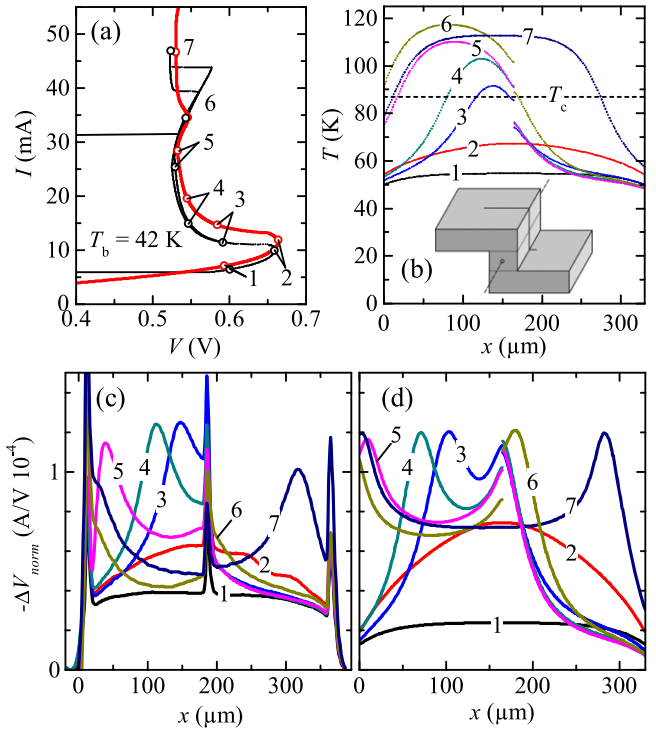

Figure 5. (a) Measured (black) and simulated (red) IVCs of the two parallel IJJ stacks at $T_b = 42$ K and (b) simulated $T(x)$-profiles taken along the line indicated in the inset, for the bias points labelled in (a). Experimental (c) and simulated (d) LTSLM voltage responses taken along the line indicated in (b).

the electrical and thermal parameters of the pristine stack. The slit in the simulations was 200 nm wide, not only separating the two stacks and the gold layer on top of them, but also fully extending into the bottom electrode. This accounts for the fact, that the FIB milling was carried out much longer than necessary, ensuring a complete division of the two stacks. The measured (black) and calculated (red) IVCs are shown in figure 5(a). Those are in qualitative agreement. However, it seems that the effect of heating is somewhat weaker in the simulated stack. Also, instead of the hysteretic region at high bias, the simulations yielded a kink slightly below 40 mA, rather than the hysteresis observed in the real sample. We note here that, for higher T_b, the hysteresis disappears in experiment and a kink similar as in the simulation is observed. Figure 5(b) shows the calculated temperature distribution for the points 1–7 on the simulated IVC. For point 1, taken in the low-bias region, there is only a weak temperature modulation and the overall temperature is only slightly above T_b. The situation is similar at bias point 2, where V is maximum, with a more elevated overall temperature. At higher currents the hot spot starts to form. Throughout the region of negative differential resistance the peak temperature of the hot spot increases, passing T_c near point 3 and reaching a value around 110 K at bias point 5. Note that the hot spot is basically confined to the left stack throughout this regime. In the regime of positive differential resistance, between points 5 and 6, the right hand tail of the hot spot notably starts to extend to the right stack and the

maximum temperature rises to more than 120 K (point 6). Above a current of 40 mA, where the voltage has decreased and the differential resistance is negative again, the hot spot has moved significantly to the right, now also occupying a big part of the right stack. We emphasize that the maximum hot-spot temperature has decreased by about 10 K, compare $T(x)$-profiles 6 and 7. Figures 5(c) and (d) compare experimental and calculated linescans of the LTSLM response for the points indicated in figure 5(a). For the comparison we have chosen the points such that the different regimes in the IVC, where the thermal behavior qualitatively changes, are covered. Note that for all points in the experimental curves there are strong edge signals that appear both near the slit and the sample edges. We will ignore them in the following discussion. Points 1 and 2 are taken in the low-bias regime and at the voltage maximum, respectively. Here, the LTSLM response is relatively smooth both in the theoretical and in the experimental curve. However, in the experimental curve at point 2 there are shallow wiggles in the right hand stack for $x > 200\,\mu$m. The wiggles arise from standing electromagnetic waves, as it has been addressed in previous publications [6, 8, 10]. The formation of the hot spot (bias point 3) and its growth (bias points 4 and 5), best seen by following the hump in the the left stack in the experimental data, is nicely reproduced by the simulation. Note, however, that in the theoretical curve both two humps are visible. In the experimental curve the right hand side hump is either obscured by the edge signal at the slit or the temperature jumps at the slit from a value well above T_c to a value well below T_c. At point 6 ΔV_{norm} in the left stack is relatively smooth due to the fact that here the temperature is basically above T_c everywhere. In the right stack there is an upturn of $-\Delta V_{\mathrm{norm}}$ near the slit indicating that also in this stack the temperature has reached T_c near its left edge. At point 7 this upturn has turned into a hump located close to the right side, i.e. also the temperature in the right stack is close to or above T_c.

3.3. Two independently biased stacks

In a second FIB milling step, the top electrode of the two stacks has been separated.

3.3.1. Electric properties and THz emission. The simplified equivalent circuit diagram is depicted in figure 1(d). The currents injected into the left stack, I_{L}, and into the right stack, I_{R}, can now be chosen independently, implying that the voltages across the two stacks can be adjusted arbitrarily. Due to the proximity of the stacks they will still interact thermally, and possibly there is also an interaction and synchronization of the Josephson currents due to electromagnetic coupling.

Figure 6(a) shows IVCs of the right stack for different currents through the left stack, which is always operated in its resistive state, except for $I_{\mathrm{L}} = 0$. The outermost branch (blue curve) in the graph corresponds to $I_{\mathrm{L}} = 0$. With increasing I_{L} the voltage across the right stack (V_{R}) decreases at given I_{R}, due to the fact that the Joule heating of the left stack also leads to a temperature rise in the right stack. Note that this

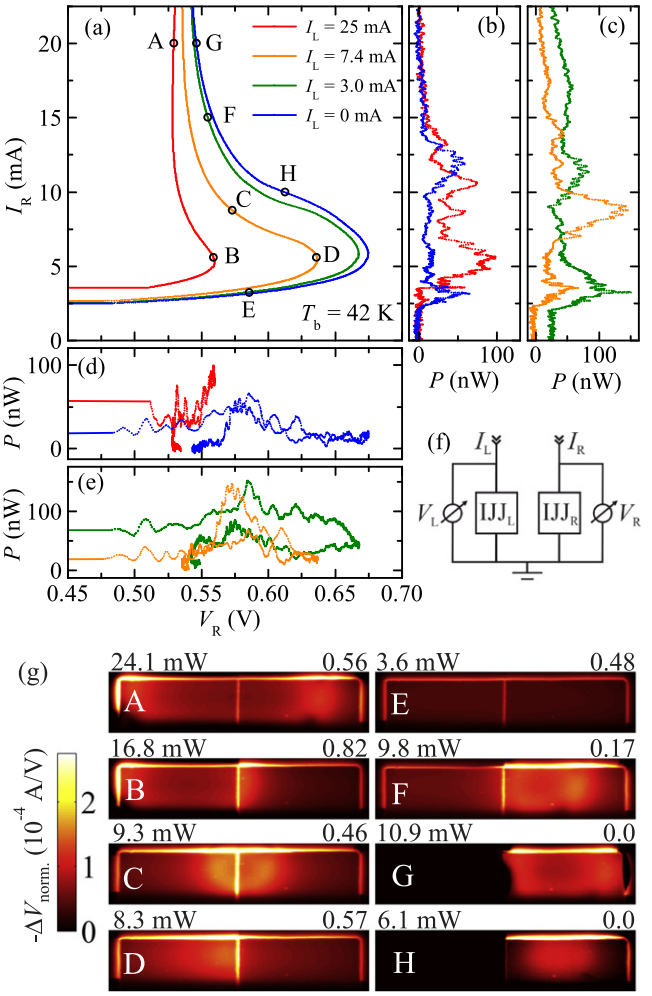

Figure 6. (a) IVC of the right stack for different currents through the left stack as indicated in the graph, while the left stack is in its resistive state (except for $I_{\mathrm{L}} = 0$). The corresponding emission signal versus current is shown in (b) and (c) and versus voltage in (d) and (e). (f) shows the equivalent electric circuit schematically. In (g) LTSLM images for the bias points indicated in (a) are shown. Values at top left of the images denote the total input power P_{DC} and at top right the current ratio $I_{\mathrm{L}}/(I_{\mathrm{L}} + I_{\mathrm{R}})$.

happens vice versa, and therefore the voltage across the left stack (V_{L}) is shifted when I_{R} is swept. The detected THz signal is shown versus I_{R} in figures 6(b) and (c) and versus V_{R} in figures 6(d) and (e). For the orange and green branch I_{L} has been chosen such that the maximum achievable emission for, respectively, high and low bias currents at this bath temperature was realized. The emission characteristics for $I_{\mathrm{L}} = 0$ resembles the behavior of the pristine stack, as two dominating emission peaks with similar voltage occur, one at low and one at high bias currents. Solely biasing the left stack leads to a similar picture. When increasing I_{L} both stacks may contribute to the emitted radiation, cf figures 6(c) and (e) for the emission power for $I_{\mathrm{L}} = 3$ mA (green) and 7.4 mA (orange).

For $I_{\mathrm{L}} = 3$ mA, the emission characteristics plotted versus I_{R} or V_{R} still look very similar as for the single stacks. However, the left stack contributes to the detected emission

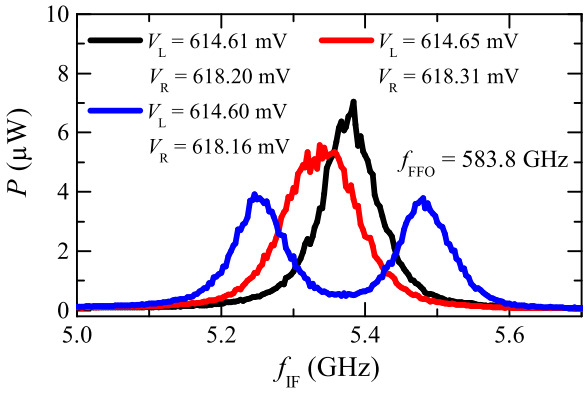

Figure 7. SIR spectra for different voltages of the two stacks. f_{FFO} is the frequency of the local oscillator.

signal, which is about 25 nW for $I_R = 0$ mA. Interestingly, this value is similar for high values of I_R, as e.g. 25 mA, where the right stack is essentially above T_c and does not contribute to the emission. However, for intermediate currents I_R and especially in the low-bias regime, both stacks contribute to the emission, leading to a quite broad low-bias emission peak with a maximum value of about 150 nW. This is roughly twice the value of the low-bias emission peak obtained for $I_L = 0$. This does not imply however, that the two stacks are synchronized (more arguments on this will be given below). Within the 15 GHz resolution of our Fourier spectrometer the emission frequency in the low-bias peak is 562 GHz and about the same as for the low-bias peaks of the left (right) stack for $I_R = 0$ ($I_L = 0$). Also, this is the same emission frequency for which the pristine stack had the maximum emission amplitude in the low-bias regime.

For $I_L = 7.4$ mA, i.e. in the high-bias regime of the left stack, where a hot spot is present, there is again one low-bias peak in $P(I_R)$ at a current and voltage position which is comparable to the case of $I_L = 0$. At $I_R = 8.8$ mA and V_R near 0.57 V a strong peak appears, which, in terms of I_R, seems to be unrelated to the peaks observed at lower values of I_L. Note, however, that the voltage position of the peak is comparable to the high-bias peak for $I_L = 0$. As we will see below, in the vicinity of this bias condition there is a hot spot which extends into both stacks and is centered in the slit between them. This may be a favorable condition for radiation.

Finally, for $I_L = 25$ mA, cf figures 6(b) and (d), the emission curves strongly differ from the $I_L = 0$ case, showing, as a function of I_R, a series of emission peaks between 5 mA and 15 mA. Here, the accessible voltage range and the sample temperatures differ significantly from the other branches, at least partly explaining this behavior.

To get more insight into the linewidth of radiation we also studied the sample after the second FIB cut using the SIR. It turned out, that the linewidth of the radiation has its minimum (approxmately 25 MHz) for T_b around 40 K, when biasing the sample in the negative differential regime, as has been observed for mesas [13]. Here, synchonization of the two stacks seems to be most promising. We tried to adjust the voltages of the stacks in this regime, while monitoring the spectra, to achieve a synchronized state. figure 7 shows typical spectra obtained for this procedure. The blue spectrum features two peaks, each coming from a different stack. A peak immediately moves in the spectrum, when the voltage of the corresponding stack is changed. For the red spectrum the two peaks already overlap strongly and seem to merge into one single peak for the black spectrum. The linewidth remains almost constant (80 MHz), when comparing the blue peaks with the black one. The sum of the amplitudes of the blue peaks, however, is more than 10% larger than the amplitude of the black peak. It seems that, at least in the present configuration, two separate stacks do not synchronize by itself without an additional mechanism. Unfortunately, the sample was destroyed before reaching the regime of the 25 MHz linewidth. However, we can state that for the configuration we studied here synchronization is at least very difficult, if not impossible.

3.3.2. Electrothermal properties. We continue with the electro-thermal behavior of the independently biased stacks. Figure 6(g) shows LTSLM images, taken at the bias points indicated by A–H in figure 6(a). The images reveal, that only *one* hot spot forms inside the two stacks, rather than two. This is a consequence of the strong thermal coupling between the two stacks due to their proximity. In other configurations, where the stacks are further apart, a hot spot forms in each stack [27]. This is an important aspect that has to be considered when designing array structures. From figure 6(g) one can also see that the hot-spot size and its position can be manipulated by adjusting the currents I_L and I_R. Roughly, one can state that a larger total input power P_{DC} increases the hot-spot size and its temperature, while the current ratio $I_L/(I_L + I_R)$ sets the position of the hot spot, similarly as in [10]. Figure 6(g) exemplarily shows some possible configurations. For $I_L = 0$ the hot spot is fully situated in the right stack, cf LTSLM images G and H. The left stack cannot provide a signal in this case. By increasing the current ratio the hot spot moves towards the left stack as shown by image F ($I_L = 3$ mA). For almost equal currents, cf image C, the hot spot is located at the center of the two stacks. By further increasing the current ratio the hot spot moves to the left stack, cf images D and B. For small P_{DC} no hot spot occurs (image E). It appears for increasing P_{DC}, cf images H and D, and occupies larger and larger areas of one (image B) or both stacks (image A). This shows, that the hot spot can be manipulated quite freely in such a structure.

Again, finite element simulations have been carried out, keeping all parameters as in the former calculations, only changing the geometry to account for the second FIB milling step. The overall electro-thermal behavior of the two independent stacks is confirmed. Figure 8(a) shows the simulated IVCs in comparison with the measured curves. Curve 1 (measured) and 2 (simulated), both for constant $I_L = 25$ mA, agree in shape, however, the simulated curve shows less pronounced heating and reaches higher voltages. The same is true for the curves with $I_L = 7.4$ and 3 mA. Although the match between simulated and measured IVCs is

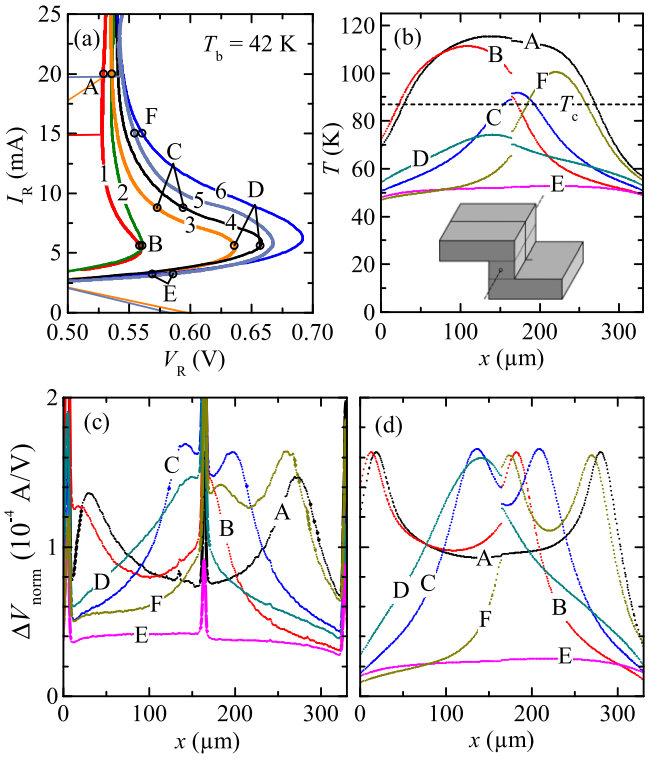

Figure 8. (a) Simulated IVCs of the right stack for I_L = 25 mA (labeled # 2), 7.4 mA (# 4) and 3 mA (# 6). The corresponding measured IVCs are, respectively, labeled by numbers 1, 3 and 5. (b) $T(x)$-profiles for the bias points indicated by letters in (a) taken along the line indicated in the inset in (b). Experimental (c) and simulated (d) LTSLM voltage responses taken along the line indicated in the inset in (b).

not perfect, the simulation adequately reproduces the shift of the IVC to lower voltages for increasing I_L. Selected $T(x)$-profiles are shown in figure 8(b), which again confirm the experimentally observed positioning and formation of the hot spot, as described by means of the LTSLM images. For completeness, also measured and simulated LTSLM linescans are shown in figures 8(c) and (d), respectively. The agreement between the measured and calculated linescans is of similar quality as before, capturing all qualitative features.

4. Discussion

In the previous section we have seen that the electro-thermal properties of the two IJJ stacks, as well as the bias points exhibiting strong THz emission, depend strongly on the electrical integration, the thermal anchoring and the biasing scheme. For example, after the first FIB cut a new hysteretic branch appeared on the IVC which was absent in the pristine structure, cf figure 3(a). Extrapolating such findings to many parallel stacks one can easily imagine that multi-stack arrangements will show a very complex behavior which will be hard to control.

In none of the arrangements of the two stacks we observed synchronized radiation, despite of the presence of interaction by the mutually impinging THz fields, by electrical currents in the superconducting electrodes or by a shared hot spot serving as a common, distributed load.At least some theoretical calculations indicated that two stacks connected in parallel, like our arrangement after the first FIB cut, should be synchronized [47, 49]. Obviously, an additional synchronization mechanism, as the cavity resonance within a single stack, seems to be necessary. In [21] and [54] synchronization was achieved for mesa structures patterned on the same base crystal, which is a lot thicker than the bottom electrode in our z-structure, suggesting that interaction via the base crystal is important. This is in line with the suggestion made in [21] and [48], that THz plasma waves in the base crystal promote synchronization. In this case, the distance between the stacks and (or) the thickness of the base crystal should be crucial parameters.

The two different stack configurations which we discussed here share the appearance of a single hot spot, a consequence of the strong thermal coupling between the stacks, which is primarily provided by the bottom electrode. A set of simulations, where we moved the stacks further apart from each other (while keeping their size constant), suggests a smooth progression from the appearance of one hot spot to the appearance of two hot spots. For a distance of 50 μm two hot spots are clearly distinguishable, almost centred in their respective stack. Reducing the distance between the stacks moves the hot spots away from their center position increasing their proximity. For 15 to 5 μm distance it gets difficult to distinguish the two hot spots and below 5 μm only one hot spot appears. It may well be advantageous for planar arrays of IJJ stacks to reduce the number of hot spots by smartly arranging the stacks: in [21] the synchronization of more than three stacks was prevented by excessive heating, which would be greatly reduced, if two to four stacks 'shared' one hot spot. At the same time it may support the synchronization amongst the IJJs within each stack [13].

5. Summary

In summary, we have investigated the electrothermal behavior and the THz emission properties of two nearby BSCCO IJJ stacks using a combination of transport and THz emission measurements plus LTSLM. The study was motivated by the fact that parallel arrays of stacks are a promising option to realize a high power superconducting THz emitter. We observed the formation of one single hot spot, which may be found in various configurations, depending on bias condition and structure of the two stacks. The impact of the respective thermal configuration on the shape of the current–voltage characteristics and the occurrence of THz emission was discussed. Further we analysed under which conditions two hot spots are to be expected. In none of the designs it was possible to achieve mutual synchronization of the two stacks, indicating that additional synchronizing elements may be necessary for the operation of parallel array structures.

Acknowledgments

We gratefully acknowledge financial support by the National Natural Science Foundation of China (Grant No. 11234006), the Priority Academic Program Development of Jiangsu Higher Education Institutions, the Deutsche Forschungsgemeinschaft (Project KL930/12-1), the Grants-in-Aid for scientific research from JSPS, RFBR grants 13-02-00493-a, 14-02-91335 and 14-02-31374, and grant No. 14.607.21.0100 by the Ministry of Education and Science of the Russian Federation.

References

[1] Darula M, Doderer T and Beuven S 1999 *Supercond. Sci. Technol.* **12** R1
[2] Barbara P, Cawthorne A B, Shitov S V and Lobb C J 1999 *Phys. Rev. Lett.* **82** 1963
[3] Song F, Müller F, Behr R and Klushin M 2009 *Appl. Phys. Lett.* **95** 172501
[4] Kleiner R, Steinmeyer F, Kunkel G and Müller P 1992 *Phys. Rev. Lett.* **68** 2394
[5] Ozyuzer L *et al* 2007 *Science* **318** 1291
[6] Wang H B, Guénon S, Yuan J, Iishi A, Arisawa S, Hatano T, Yamashita T, Koelle D and Kleiner R 2009 *Phys. Rev. Lett.* **102** 017006
[7] Kurter C, Ozyuzer L, Proslier T, Zasadzinski J F, Hinks D G and Gray K E 2010 *Phys. Rev.* B **81** 224518
[8] Wang H B *et al* 2010 *Phys. Rev. Lett.* **105** 057002
[9] Tsujimoto M, Yamaki K, Deguchi K, Yamamoto T, Kashiwagi T, Minami H, Tachiki M, Kadowaki K and Klemm R A 2010 *Phys. Rev. Lett.* **105** 037005
[10] Guenon S *et al* 2010 *Phys. Rev.* B **82** 214506
[11] Benseman T M, Koshelev A E, Gray K E, Kwok W-K, Welp U, Kadowaki K, Tachiki M and Yamamoto T 2011 *Phys. Rev.* B **84** 064523
[12] Yuan J *et al* 2012 *Supercond. Sci. Technol.* **25** 075015
[13] Li M *et al* 2012 *Phys. Rev.* B **86** 060505
[14] Tsujimoto M *et al* 2012 *Phys. Rev. Lett.* **108** 107006
[15] Tsujimoto M, Minami H, Delfanazari K, Sawamura M, Nakayama R, Kitamura T, Yamamoto T, Kashiwagi T, Hattori T and Kadowaki K 2012 *J. Appl. Phys.* **111** 123111
[16] Kakeya I, Omukai Y, Yamamoto T, Kadowaki K and Suzuki M 2012 *Appl. Phys. Lett.* **100** 242603
[17] Kashiwagi T *et al* 2012 *Japan J. Appl. Phys.* **51** 010113
[18] Turkoglu F, Koseoglu H, Demirhan Y, Ozyuzer L, Preu S, Malzer S, Simsek Y, Müller P, Yamamoto T and Kadowaki K 2012 *Supercond. Sci. Technol.* **25** 125004
[19] An D Y *et al* 2013 *Appl. Phys. Lett.* **102** 092601
[20] Benseman T M, Koshelev A E, Kwok W-K, Welp U, Vlasko-Vlasov V K, Kadowaki K, Minami H and Watanabe C 2013 *J. Appl. Phys.* **113** 133902
[21] Benseman T M, Gray K E, Koshelev A E, Kwok W-K, Welp U, Minami H, Kadowaki K and Yamamoto T 2013 *Appl. Phys. Lett.* **103** 022602
[22] Benseman T M, Koshelev A E, Kwok W-K, Welp U, Kadowaki K, Cooper J R and Balakrishnan G 2013 *Supercond. Sci. Technol.* **26** 085016
[23] Sekimoto S, Watanabe C, Minami H, Yamamoto T, Kashiwagi T, Klemm R A and Kadowaki K 2013 *Appl. Phys. Lett.* **103** 182601
[24] Gross B *et al* 2013 *Phys. Rev.* B **88** 014524
[25] Minami H, Watanabe C, Sato K, Sekimoto S, Yamamoto T, Kashiwagi T, Klemm R A and Kadowaki K 2014 *Phys. Rev.* B **89** 054503
[26] Kashiwagi T *et al* 2014 *Appl. Phys. Lett.* **104** 082603
[27] Watanabe C, Minami H, Yamamoto T, Kashiwagi T, Klemm R A and Kadowaki K 2014 *J. Phys.: Condens. Matter* **26** 172201
[28] Koshelev A E and Bulaevskii L N 2008 *Phys. Rev.* B **77** 014530
[29] Koshelev A E 2008 *Phys. Rev.* B **78** 174509
[30] Lin S and Hu X 2008 *Phys. Rev. Lett.* **100** 247006
[31] Krasnov V M 2009 *Phys. Rev. Lett.* **103** 227002
[32] Tachiki M, Fukuya S and Koyama T 2009 *Phys. Rev. Lett.* **102** 127002
[33] Pedersen N and Madsen S 2009 *IEEE Trans. Appl. Supercond.* **19** 726
[34] Lin S-Z and Hu X 2010 *Phys. Rev.* B **82** 020504
[35] Krasnov V M 2010 *Phys. Rev.* B **82** 134524
[36] Koshelev A E 2010 *Phys. Rev.* B **82** 174512
[37] Koyama T, Matsumoto H, Machida M and Ota Y 2011 *Supercond. Sci. Technol.* **24** 085007
[38] Krasnov V M 2011 *Phys. Rev.* B **83** 174517
[39] Yurgens A 2011 *Phys. Rev.* B **83** 184501
[40] Yurgens A and Bulaevskii L N 2011 *Supercond. Sci. Technol.* **24** 015003
[41] Asai H, Tachiki M and Kadowaki K 2012 *Phys. Rev.* B **85** 064521
[42] Lin S-Z and Hu X 2012 *Phys. Rev.* B **86** 054506
[43] Averkov Y O, Yakovenko V M, Yampolskii V A and Nori F 2012 *Phys. Rev. Lett.* **109** 027005
[44] Gross B *et al* 2012 *Phys. Rev.* B **86** 094524
[45] Asai H and Kawabata S 2014 *Appl. Phys. Lett.* **104** 112601
[46] Grib A and Seidel P 2014 *Phys. Stat. Solidi* B **251** 1040
[47] Lin S Z 2014 *J. Appl. Phys.* **115** 173901
[48] Lin S-Z and Koshelev A E 2013 *Physica C* **491** 24
[49] Shukrinov Y M, Rahmonov I R, Plecenik A, Seidel P, Il'ichev E and Nawrocki W 2014 *Supercond. Sci. Technol.* **27** 124007
[50] Welp U, Kadowaki K and Kleiner R 2013 *Nat. Photonics* **7** 702
[51] Kawayama I, Zhang C, Wang H B and Tonouchi M 2013 *Supercond. Sci. Technol.* **26** 093002
[52] Gurevich A V and Mints R G 1987 *Rev. Mod. Phys.* **59** 941
[53] Ji M *et al* 2014 *Appl. Phys. Lett.* **105** 122602
[54] Orita N, Minami H, Koike T, Yamamoto T and Kadowaki K 2010 *Physica* C **470** S786
[55] Wang H B, Wu P H, Chen J, Maeda K and Yamashita T 2002 *Appl. Phys. Lett.* **80** 1604
[56] Wang H B *et al* 2009 *Phys. Rev.* B **80** 224507
[57] Koshelets V P, Ermakov A B, Filippenko L V, Kinev N V, Kiselev O S, Torgashin M Y, de Lange A, de Lange G, Pripolzin S I and Vaks V L 2010 *Proc. SPIE* **7854** 78540J
[58] Spenke E 1935 *Electr. Eng. (Arch. fuer Elektrotech.)* **30** 728
[59] Spenke E 1936 *Wiss. Verff. a. d. Siemens-Werken* **15** 92